HEAT TRANSFER THROUGH A CONDENSATE DROPLET ON HYDROPHOBIC AND NANOSTRUCTURED SUPERHYDROPHOBIC SURFACES

BY

SHREYAS CHAVAN

THESIS

Submitted in partial fulfillment of the requirements
for the degree of Master of Science in Mechanical Engineering
in the Graduate College of the
University of Illinois at Urbana-Champaign, 2016

Urbana, Illinois

Adviser:

Assistant Professor Nenad Miljkovic

ABSTRACT

Understanding the fundamental mechanisms governing vapor condensation on non-wetting surfaces is crucial to a wide range of energy and water applications. In this thesis, we reconcile classical droplet growth modeling barriers by utilizing two-dimensional axisymmetric numerical simulations to study individual droplet heat transfer on non-wetting surfaces ($90° < \theta_a < 170°$). Incorporation of an appropriate convective boundary condition at the liquid vapor interface reveals that the majority of heat transfer occurs at the three phase contact line, where the local heat flux can be up to 4 orders of magnitude higher than at the droplet top. Droplet distribution theory is incorporated to show that previous modeling approaches under predict the overall heat transfer by as much as 300% for dropwise and jumping-droplet condensation. To verify our simulation results, we study condensed water droplet growth using optical and ESEM microscopy on bi-philic samples consisting of hydrophobic and nanostructured superhydrophobic regions, showing excellent agreement with the simulations for both constant base area and constant contact angle growth regimes. Our results demonstrate the importance of resolving local heat transfer effects for the fundamental understanding and high fidelity modeling of phase change heat transfer on non-wetting surfaces.

ACKNOWLEDGMENTS

The author wishes to express sincere appreciation to Professor Nenad Miljkovic, for his constant support and guidance during the course of this project. In addition, special thanks to the members of Energy Transport Research Lab, especially Patrick Birbarah, Nitish Singla, Deokgeun Park, Yip Fun Yeung, Dong Hoon Kang and Yujin Chang for their help with the simulations and experimental setup.

I acknowledge funding support from the Air Conditioning and Refrigeration Center (ACRC), an NSF-founded I/UCRC at UIUC. I also acknowledge the support of the International Institute for Carbon Neutral Energy Research (WPI-I2CNER), sponsored by the Japanese Ministry of Education, Culture, Sports, Science and Technology. Electron microscopy was carried out in part in the Frederick Seitz Materials Research Laboratory Central Facilities, University of Illinois.

Finally, I am grateful to my family, my mother, my father, and my younger sister for their constant motivation and confidence in me. They are the reason for what I am today.

TABLE OF CONTENTS

LIST OF SYMBOLS

h_{i}	Heat transfer coefficient at liquid-vapor interface (m)
h_{fg}	latent heat of vaporization (J/kg)
$\hat{R}$	effective maximum droplet radius (m)
R_{b}	Droplet base radius (m)
R_{e}	droplet coalescence radius (m)
R_{g}	specific gas constant (J/mol K)
R_{min}	minimum droplet nucleation radius (m)
R_{t}	overall droplet thermal resistance (K/W)
T_{i}	Temperature at liquid-vapor interface (K)
T_{s}	substrate/wall temperature (K)
k_{HC}	hydrophobic promoter coating thermal conductivity (W/mK)
k_{p}	pillar/substrate thermal conductivity (W/m K)
k_{w}	water thermal conductivity (W/m K)
δ_{HC}	thickness of hydrophobic coating (m)
θ_a	advancing contact angle (deg)
ν_{g}	water vapor specific volume (m^3/kg)
ρ_{w}	water density (kg/m^3)
$\Delta T = T_{sat} - T_s$	surface subcooling temperature (K)
h	pillar height (m)
q″	heat flux through the droplet (W/m^2)
Bi	Biot Number
N	large droplet population density (m^{-3})
Nu	Nusselt number
R	Radius of the spherical droplet
n	small droplet population density (m^{-3})
α	condensation coefficient

θ	contact angle (deg)
τ	sweeping period (s)
ϕ	solid fraction

CHAPTER 1: INTRODUCTION

Water vapor condensation is routinely observed in nature and has a large influence on the performance of engineered systems such as building environmental control,[1-3] power generation,[4] and high-heat-flux thermal management.[5] Previous studies have shown that water vapor condensation on hydrophobic surfaces has a 5-10X enhanced condensation heat transfer performance when compared hydrophilic surfaces, due to the formation and rapid removal of discrete condensate droplets from the surface *via* gravity (shedding).[6-10] The former, termed 'dropwise' condensation,[11] has been the topic of vigorous investigation since its discovery 80 years ago. With the aim of further enhancing droplet shedding, researchers have recently developed ultra-low adhesion superhydrophobic surfaces,[12, 13] and discovered that when microdroplets (~10-100 μm) condense and coalesce, the resulting droplet can jump away from the surface irrespective of gravity due to surface-to-kinetic energy transfer.[14-19] This phenomenon has been termed jumping-droplet condensation and has been shown to further enhance heat transfer by up to 30% when compared to dropwise condensation.[20] A number of works have since fabricated superhydrophobic nanostructured surfaces to achieve spontaneous droplet removal[21] for a variety of applications including self-cleaning,[22-24] thermal diodes,[23, 25] anti-icing,[26-29] vapor chambers,[30] electrostatic energy harvesting,[31-33] and condensation heat transfer enhancement.[34-45]

Although experimental studies of dropwise and jumping-droplet condensation on superhydrophobic surfaces have advanced significantly over the past decade, modeling of the heat transfer process has lagged. Specifically, individual droplet heat transfer dynamics are poorly understood and cannot be computed accurately by using the simplifying assumption of constant temperature boundary conditions on the droplet base (solid-liquid interface) and free surface (liquid-vapor interface).[6, 8, 20, 37, 39, 46-51] First identified 50 years ago,[52] this discrepancy has been reconciled *via* detailed three-dimensional simulations of droplets residing on hydrophilic surfaces ($15° < \theta_a < 90°$) by assuming a convective boundary condition with a finite heat transfer coefficient on the free surface.[53-55] However, little attention has been paid to droplets growing on hydrophobic ($90° < \theta_a < 150°$) or superhydrophobic ($150° < \theta_a < 180°$) surfaces from a simulation standpoint. Given the recent discovery of jumping-droplet condensation, work is needed to study droplet condensation heat transfer on superhydrophobic substrates having advancing contact angles greater than 90°.

In this work, we develop a two-dimensional (2D) axisymmetric numerical simulation of the individual droplet heat transfer on hydrophobic and superhydrophobic surfaces to study droplets of arbitrary contact angle ($90° < \theta_a < 170°$). The local droplet heat flux and temperature are computed and expressions for the droplet Nusselt number as a function of the Biot number and apparent advancing contact angle are presented, showing excellent agreement with the previously derived analytical solution for hemispherical droplets ($\theta_a = 90°$). Using

our simulation results, we demonstrate that the majority of the heat transfer during condensation on superhydrophobic surfaces occurs at the three phase contact line, and that local heat transfer and temperature effects must be considered when computing condensation heat transfer on superhydrophobic surfaces due to their large interfacial temperature variation and minimal contact area with the substrate. To verify our simulations, we performed optical microscopy studies of water vapor condensation in the presence of non-condensables on macroscopically bi-philic copper samples having simultaneous hydrophobic ($\theta_a \approx 140°$) and superhydrophobic ($\theta_a \approx 170°$) droplet growth morphologies. To elucidate the effects of non-condensables, we also performed Environmental Scanning Electron Microscopy (ESEM) of water vapor condensation on superhydrophobic ($\theta_a \approx 170°$) and hydrophobic ($\theta_a \approx 120°$) surfaces. The numerical simulations showed excellent agreement with the experimental results under identical supersaturations and for both constant basal area and constant contact angle growth regimes. Furthermore, the experimental results indicate that the critical supersaturation does not uniquely define the initiation of nucleation mediated flooding on a structured surface, rather condensation heat flux is a better metric. The outcomes of this work elucidate the heat transfer physics governing individual droplet growth during water vapor condensation on both hydrophobic and superhydrophobic surfaces that can be extended to the study of droplet-basal contact resistance on microstructured surfaces, evaporation, and freezing processes in energy and water applications.

CHAPTER 2: MODEL

2.1 Non dimensional analysis

Consider the system of a condensing water droplet on a superhydrophobic surface as shown in Figure 2.1. Using Buckingham Pi theorem,[56] we can reduce the number of explicit physical variables to a reduced number of dimensionless parameters.

The number of physical variables defining the system are $m = 7$ [R, T_{sat}, T_s, q'', k_w, h_i, θ_a]. Meanwhile, the number of physical dimensions, $n = 4$ [L, M, θ, T]. Therefore, the number of dimensionless groups which define the system can be represented by $\Pi = m - n = 3$. Since θ_a is already dimensionless, we define it as our first dimensionless group, $\Pi_1 = \theta_a$.

For the second dimensionless group, we use R_b, k_w, h_i, to non-dimensionalize the problem.

h_i	$Wm^{-2}K^{-1}$	$[M\ \theta^{-1}\ T^{-3}]$
k_w	$Wm^{-1}K^{-1}$	$[L\ M\ \theta^{-1}\ T^{-3}]$
R_b	m	[L]

Using the Buckingham Π theorem, we get,

$$[M\theta^{-1}T^{-3}][LM\theta^{-1}T^{-3}]^a[L]^b = 1 \qquad (2.1)$$

Solving, we obtain $a = -1, b = 1$, therefore:

$$\Pi_2 = Bi = \frac{h_i R_b}{k_w} \tag{2.2}$$

For the third dimensionless group, we use q'', R, k_w, ΔT to non-dimensionalize:

k_w	W/mK	$[L^{-1}\ M\ \theta^{-1}\ T^{-3}]$
q''	W/m^2	$[M\ T^{-3}]$
R_b	m	[L]
ΔT	K	[θ]

Using the Buckingham Π theorem, we get,

$$[MT^{-3}][L]^a[\theta]^b[L^{-1}M\theta^{-1}T^{-3}]^c = 1 \tag{2.3}$$

Solving, we obtain $a = -1, b = -1, c = -1$

$$\Pi_3 = Nu = \frac{q''}{k_w R_b \Delta T} \tag{2.4}$$

Using Buckingham Π theorem, we can write

$$\Pi_3 = f(\Pi_2, \Pi_1) \tag{2.5}$$

Thus,

$$Nu = f(Bi, \theta_a) \tag{2.6}$$

2.2 ANSYS Setup

To study the individual droplet heat transfer process, a 2D axisymmetric numerical model based on the finite element method was used to solve the heat equation through a single droplet. Although the droplet heat transfer process during condensation is exceedingly complex, some simplifying assumptions are possible from realizing that most of the heat is transferred through droplets of diameter less than 100 μm.[37, 57] For such small droplets the influence of gravity on the droplet shape is negligible and a spherical-segment geometry may be assumed (Figure 2.1). In addition, Marangoni and buoyant convection are neglected since the droplets are sufficiently small so that conduction is the dominant mode of heat transfer.[58, 59] Furthermore, the heat transfer and droplet growth are quasi-steady processes governed by the steady heat-conduction equation, ensuring that an analytic formulation can be completed with various boundary conditions.[53]

Quadrilateral meshing was used as shown in Figure 2.2 with 10,000 nodes. The ratio of maximum element size to the droplet radius was taken to be 0.015. Mesh refinement was used at the liquid-vapor interface and solid-liquid interface (ratio of element size to the droplet radius being 0.008). Mesh at the three phase contact line was further refined (ratio of element size to the droplet radius being 0.004) to capture the large temperature gradients present there. To reduce computation time, a 2D axis symmetry model was simulated.

The ratio of maximum element size to droplet radius used in all the simulations was 0.015. This ratio was chosen because decreasing the mesh size beyond this point resulted in less than 1% change in the result as shown in Figure 2.3.

To reconcile the discontinuity associated with a constant free surface temperature, we assume a constant heat transfer coefficient boundary condition at the liquid-vapor interface, and a constant droplet-surface interface temperature (T_s). The liquid-vapor interface heat transfer coefficient is given by the interfacial condensation heat transfer coefficient, h_i:[60]

$$h_i = \frac{2\alpha}{2-\alpha}\frac{1}{\sqrt{2\pi R_g T_{sat}}}\frac{h_{fg}^2}{v_g T_{sat}}, \tag{2.7}$$

where R_g is the specific gas constant and v_g is the water vapor specific volume, T_{sat} is the water vapor saturation temperature, and h_{fg} is the latent heat of condensation phase change. The condensation coefficient α is the ratio of vapor molecules that will be captured by the liquid phase to the total number of vapor molecules reaching the liquid surface (ranging from 0 to 1). In order to study the effect of condensation coefficient on heat transfer, the model was simulated for different values of α (0.01, 0.04, and 1), representing both contaminated (α = 0.01) and clean (α = 1) environments.[52]

The condensate droplet is assumed to have a constant apparent advancing contact angle (θ_a). This assumption places constraints on the maximum structure length scale beneath the droplet since only nanostructured surfaces result in both 1) droplets with constant contact angle at an early stage of droplet growth (R ~ 100 nm)[15, 37] and 2) negligible thermal resistance beneath the droplet.[39] Hence, this assumption is well suited for droplets growing on smooth hydrophobic surfaces ($90° < \theta_a < 125°$),[10] as well as nanostructured superhydrophobic surfaces.[20, 37]

For the analysis, the ambient temperature was assumed to be at saturation, T_{sat} = 100°C. The solid-liquid interface was assumed to be at a constant temperature, T_s = 90°C. This assumption is valid given the high thermal conductivity of the substrate.[53] The saturation (T_{sat}) and surface (T_s) temperatures were varied to study the effect on overall droplet thermal resistance (R_t). As expected, the results showed that R_t was independent of $\Delta T = T_{sat} - T_s$.

Non-dimensional analysis of the simulation parameters reveals three fundamental dimensionless groups governing the droplet heat transfer behavior. The individual droplet heat transfer, characterized by the droplet Nusselt number (Nu), is a function of the Biot number (Bi) and apparent advancing contact angle (θ_a), *i.e.* $Nu = f(Bi, \theta_a)$. Here, the Nusselt and Biot numbers are defined in terms of the droplet base radius (R_b) as: [53]

$$Bi = \frac{h_{\mathrm{i}} R_{\mathrm{b}}}{k_{\mathrm{w}}}, \tag{2.8}$$

$$Nu = \frac{Q}{k_{\mathrm{w}} R_{\mathrm{b}} (T_{\mathrm{sat}} - T_{\mathrm{s}})}, \tag{2.9}$$

where Q is the total heat transfer through the droplet and k_{w} is the droplet thermal conductivity.

In order to access a wide parameter space, numerical simulations were conducted for: T_{s} = 90°C, T_{sat} = 100°C, 90° < θ_{a} < 170°, and 0.1 < Bi < 10^5 (corresponding to droplet base radii: 3.19 nm < R_b < 3.19 mm for $\alpha = 1$). Convergence of the heat transfer simulation was based on the norm of the Newton-Raphson load, with a tolerance of 0.001 and a minimum reference value of 1E-06.

2.3 Condensation heat transfer calculations

To study the overall steady-state condensation heat flux, we combined the simulation results with droplet distribution theory to account for the fraction of droplets on the surface of a given radius R for the surfaces undergoing shedding and jumping. For small droplets ($R \leq R_{\mathrm{e}}$), the size distribution $n(R)$ is determined by:[47]

$$n(R) = \frac{1}{3\pi R_{\mathrm{e}}^3 \hat{R}} \left(\frac{R_{\mathrm{e}}}{\hat{R}}\right)^{-\frac{2}{3}} \frac{R(R_{\mathrm{e}} - R_{\mathrm{min}})}{R - R_{\mathrm{min}}} \frac{A_2 R + A_3}{A_2 R_{\mathrm{e}} + A_3} \exp(B_1 + B_2) \tag{2.10}$$

where, where $\hat{R}$ is the average maximum droplet radius (departure radius), R_{e} is the radius when droplets growing by direct vapor addition begin to merge and grow by droplet coalescence, $R_{\min}$ is the critical nucleation radius for condensing droplets (≈10 nm for water). For large droplets ($R \geq R_{\mathrm{e}}$) growing due to coalescence, the droplet distribution $N(R)$ is determined from:[7]

$$N(R) = \frac{1}{3\pi R_{\mathrm{e}}^2 \hat{R}} \left(\frac{R_{\mathrm{e}}}{\hat{R}}\right)^{-\frac{2}{3}} \tag{2.11}$$

The variables A_1, A_2, A_3, B_1, B_2 are constants associated with droplet sweeping, defined as:[39]

$$A_1 = \frac{\Delta T}{h_{fg}\rho_w (1-\cos\theta)^2 (2+\cos\theta)} \tag{2.12}$$

$$A_2 = \frac{\theta}{4k_w \sin\theta} \tag{2.13}$$

$$A_3 = \frac{1}{2h_i(1-\cos\theta)} + \frac{1}{k_{HC}\sin^2\theta}\left[\frac{k_p\phi}{\delta_{HC}k_p + hk_{HC}} + \frac{k_p(1-\phi)}{\delta_{HC}k_w + hk_{HC}}\right]^{-1} \tag{2.14}$$

$$B_1 = \frac{A_2}{\tau A_1}\left[\frac{R_e^2 - R^2}{2} + R_{min}(R_e - R) - R_{min}^2 \ln\left(\frac{R - R_{min}}{R_e - R_{min}}\right)\right] \tag{2.15}$$

$$B_2 = \frac{A_3}{\tau A_1}\left[R_e - R - R_{min}\ln\left(\frac{R - R_{min}}{R_e - R_{min}}\right)\right] \tag{2.16}$$

$$\tau = \frac{3R_e^2(A_2R_e + A_3)^2}{A_1(11A_2R_e^2 - 14R_eR_{min} + 8A_3R_e - 11A_3R_{min})} \tag{2.17}$$

In our case, the analysis is valid for smooth hydrophobic surfaces (ϕ = 1, h = 0, $\delta_{HC} \approx 0$) or nanostructured superhydrophobic surfaces ($h \approx 0$, $\delta_{HC} \approx 0$), A_3 is defined as:

$$A_3 = \frac{1}{2h_i(1 - \cos\theta)} \tag{2.18}$$

The total surface steady state condensation heat flux (q") is obtained by incorporating the individual droplet heat transfer rate obtained from simulations, with the droplet size distributions (Equation (2.10) and (2.11)):

$$q" = \int_{R_{\min}}^{R_e} Q(R)n(R)dR + \int_{R_e}^{\hat{R}} Q(R)N(R)dR \tag{2.19}$$

2.4 Figures

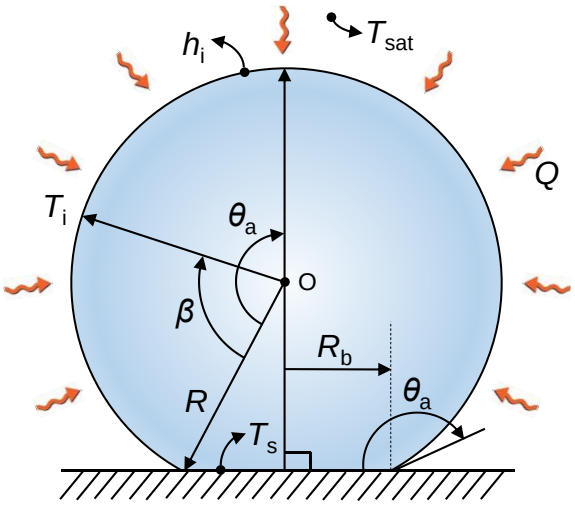

Figure 2.1. Schematic of the simulation domain showing a condensate droplet with radius (R), base radius (R_b), and advancing contact angle (θ_a). The boundary conditions are: 1) constant base (liquid-solid interface) temperature (T_s), 2) constant vapor temperature (T_{sat}), and 3) constant interfacial heat transfer coefficient (h_i) at the free surface (liquid-vapor interface). The heat conduction equation ($\nabla^2 T = 0$) governs the heat transfer inside the 3D droplet, and Marangoni and buoyancy convection are not considered due to the small droplet radii considered in these simulations.

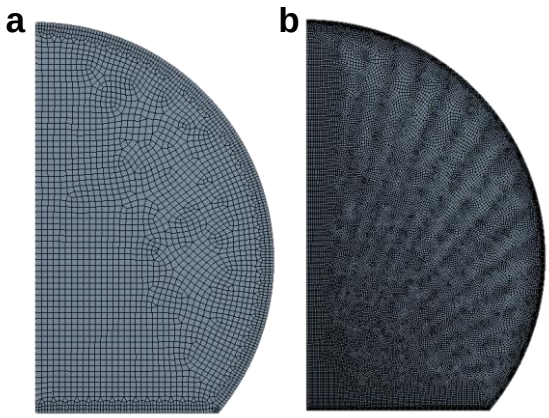

Figure 2.2. Quadrilateral mesh used to model the droplet showing with ratio of maximum element size to droplet radius of (a) 0.06, and (b) 0.015. The differing ratios were used to prove grid independence and convergence of the solution to a single answer.

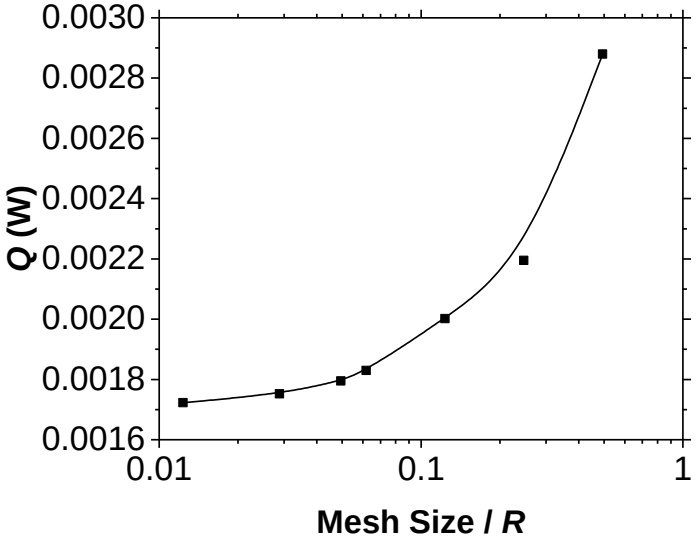

Figure 2.3. Droplet heat transfer as a function of mesh size for $\theta_a = 140^{\circ}$ and $Bi = 100$.

CHAPTER 3: SIMULATION RESULTS

3.1 Liquid-Vapor Interfacial Temperature and Heat Flux as a Function of Interface Location

Figure 3.1 shows the liquid-vapor interfacial temperature (T_i) and heat flux (q") as a function of interface location (β) from the three phase contact line for (a, b) θ_a = 120° and (c, d) θ_a = 170°. Droplets having low Bi ($Bi \rightarrow 0.1$, $R_b \rightarrow 157$ nm for condensation coefficient, $\alpha = 0.04$) showed smaller temperature gradients at the three phase contact line when compared to droplets with high Bi ($Bi \rightarrow 100$, $R_b \rightarrow 157$ µm for condensation coefficient, $\alpha = 0.04$). A small condensation coefficient, $\alpha = 0.04$ was used for these simulations to better display of gradient of T_i and q" for a given Bi. The efficient heat transfer of small droplets results in higher vapor-to-free-surface temperature difference ($T_{sat} - T_i$) due to the low conduction pathway though the droplet itself ($Q_{conduction} = Q_{interface} \sim h_i(T_{sat} - T_i)$), and hence lower temperature gradients. The interfacial heat flux (Figure 3.1b and d)) is very non-uniform and peaks at the three-phase contact line due to the efficient heat path from the liquid-vapor interface to the droplet base. Small droplets ($Bi \rightarrow 0.1$) exhibited higher local heat fluxes when compared to their larger counterparts ($Bi \rightarrow 100$) due to the low droplet conduction resistance, meanwhile larger droplets having elevated contact angles ($\theta_a \rightarrow 180°$) showed significant heat flux degradation due to the poor heat transfer characteristics caused by the limited droplet basal area (Figure 3.1d). The results show that the local heat flux can vary

as much as 4 orders of magnitude from the three phase contact line to the droplet top, indicating the importance of resolving the local heat transfer in order to obtain high fidelity results.

3.2 Nusselt Number as a Function of Contact Angle and Biot Number

To further quantify the droplet heat transfer, the simulation results were used to calculate the droplet Nusselt number (Nu, Equation (3)). Figure 3.2 shows Nu as a function of θ_a for different Bi. For small droplets ($Bi < 5$), Nu increases with increasing θ_a due to the low conduction resistance as well as higher interfacial heat transfer area associated with higher θ_a. However, for large droplets ($Bi > 5$), Nu decreases with increasing θ_a due to the elevated conduction resistance associated with higher θ_a, indicating that droplets with $Bi < 5$ are interface limited, while droplets having $Bi > 5$ are conduction limited. A comparison of the results shown in Figure 3.2 with those obtained by a previous study analyzing droplet heat transfer on a hydrophilic surface ($0 < \theta_a < 90°$) using differential inequalities,[53] shows excellent agreement at $\theta_a = 90°$. It is also interesting to see that for $Bi \approx 5$, the Nusselt number is almost invariant ($Nu \approx 8$) with the advancing contact angle and, hence, experiments which are independent of θ_a can be performed. Furthermore, the constant Nu result indicates the critical droplet size where the interfacial heat transfer resistance is approximately equivalent to the droplet conduction resistance, which for the case of $\theta_a \approx 170°$ equates to a droplet size of $R \approx 1$ μm (for condensation coefficient, $\alpha = 1$), in good agreement with previous

experimental work identifying the growth regime crossover for conduction resistance on superhydrophobic surfaces.[37]

It is important to note that the heat transfer results relating Nu to θ_a and Bi (Figure 3.2) are universal and independent of condensation coefficient (α) and vapor-to-surface temperature difference ($\Delta T = T_{sat} - T_s$). This behavior was expected since the Nusselt number (Nu), Biot number (Bi) and apparent advancing contact angle (θ_a) are the three dimensionless parameters that completely define the system.

In order to provide the best fit estimate for $Nu = f(Bi, \theta_a)$, and to provide an analytical result that can more easily be integrated into droplet growth and phase change heat transfer models, the results of Figure 3.2 were fitted using the least squares method to obtain the following expressions (θ_a is in radians) with a mean and maximum error of 4% and 23%, respectively:

$$Nu = 3{\theta_a}^{0.65} Bi^{0.83} + 0.007{\theta_a}^{5.1} Bi^{-0.23} \qquad Bi \leq 0.5 \qquad (3.1)$$

$$Nu = 0.29{\theta_a}^{2.24} Bi^{-0.17} + 3.33{\theta_a}^{-0.3} Bi^{0.72} \qquad 0.5 < Bi \leq 2 \qquad (3.2)$$

$$Nu = 5.76e^{-0.28{\theta_a}^{0.68}} \ln(1 + 5Bi^{0.82} - 2.79Bi^{0.83}) \qquad 2 < Bi \leq 10^5 \qquad (3.3)$$

To account for the droplet vapor pressure increase with decreasing droplet size (increasing curvature) we altered the vapor-to-surface temperature difference

in our numerical model. The vapor-to-surface temperature decrease due to droplet curvature is given by:

$$\Delta T_{\mathrm{c}} = \frac{R_{\min}}{R}(T_{\mathrm{sat}} - T_{\mathrm{s}}) = \frac{2T_{\mathrm{sat}}\sigma}{Rh_{\mathrm{fg}}\rho_{\mathrm{w}}}, \tag{3.4}$$

where $R_{\min}$ is the critical nucleation radius for condensing droplets (≈10 nm for water in laboratory conditions), and σ and ρ_{w} are the condensate surface tension and density, respectively. Figure 3.3 shows $Nu = f(Bi, \theta_{\mathrm{a}})$ for the numerical simulation with and without the curvature resistance included. As observed from Figure 3.3, and Equation (7), the curvature resistance decreases as droplet size increases and becomes negligible for $Bi \geq 5$ ($R_b \approx 0.16$ μm for $\alpha = 1$), hence its inclusion in the exact numerical simulation resulted in negligible changes in heat transfer behavior.

3.3 Overall Thermal Resistance

To compare the results of our numerical simulation to the state-of-the art (SoA) analytical solution,[39, 47] we define the overall droplet thermal resistance as: $R_{\mathrm{t}} = (T_{\mathrm{sat}} - T_{\mathrm{s}})/Q$. The droplet thermal resistance includes the interfacial heat transfer resistance due to the difficulty of isolating the droplet conduction resistance (non-constant free-surface temperature). Figure 3.4 shows the numerical and analytical droplet thermal resistance as a function of θ_{a} for different Bi. Both the numerical and analytical solutions show excellent agreement at low Bi ($Bi < 5$)

however the solutions deviate significantly as Bi increases (Bi > 5) due to the higher error associated with the analytical method for larger droplets. At low droplet radii (Bi < 5), the interfacial heat transfer resistance dominates both solutions, hence the good agreement is observed. As the droplet radius increases (Bi > 5), the droplet growth becomes conduction limited and the discrepancy between the two methods becomes apparent. From a physical standpoint, the smaller thermal resistance of the numerical solution stems from its ability to capture local heat transfer effects at the three phase contact line. As shown in Figure 3.1, the three phase contact line acts as a heat transfer channel during condensation of large droplets (Bi > 5) due to the low heat diffusion distance. Currently used analytical approaches using conduction shape factor solutions cannot reconcile these details, resulting in low-fidelity results.

3.4 Total Surface Steady State Condensation Heat Flux

The total surface steady state condensation heat flux (q") is obtained by incorporating the individual droplet heat transfer rate obtained from simulations (Equation 4-6), with the droplet size distributions (Equation 8, 9):

$$q" = \int_{R_{\min}}^{R_e} Q(R)n(R)dR + \int_{R_e}^{\hat{R}} Q(R)N(R)dR \tag{3.5}$$

Figure 3.5 shows the steady-state condensation heat flux as a function of θ_a for dropwise and jumping-droplet removal mechanisms. For both the numerical

and analytical solutions, increasing θ_a results in decreased heat transfer performance due to the formation of droplets which are more spherical and have higher conduction thermal resistances through them. Although experimentally, surfaces having elevated contact angles necessitate greater non-wetting and smaller contact angle hysteresis, the hysteresis was kept constant in these simulations to simplify the model. The jumping-droplet condensation heat transfer coefficient was ≈40% higher than that of dropwise condensation, in excellent agreement with previous experimental studies.[61] Interestingly, a significant difference in the condensation heat flux can be observed between the analytical and numerical solutions. For dropwise condensation, the difference is as large as 300%, which stems from the inability of the analytical solution to capture the local heat transfer behavior at the three phase contact line. Furthermore, dropwise condensation is typified by the formation of large droplets (≈2 mm for water) prior to shedding, resulting in a considerable fraction of droplets having $Bi > 5$, where the analytical and numerical models have been shown to diverge (Figure 3.4). Conversely, the jumping droplet condensation results had a relatively smaller deviation between the analytical and numerical results. This was mainly due to jumping-droplet condensation being characterized with a large population of small microdroplets (≈ 10 μm) having $Bi < 5$, where the droplet growth is interface limited and conduction resistance through the droplet, and any three-phase contact line effects, are not as pronounced.

3.5 Figures

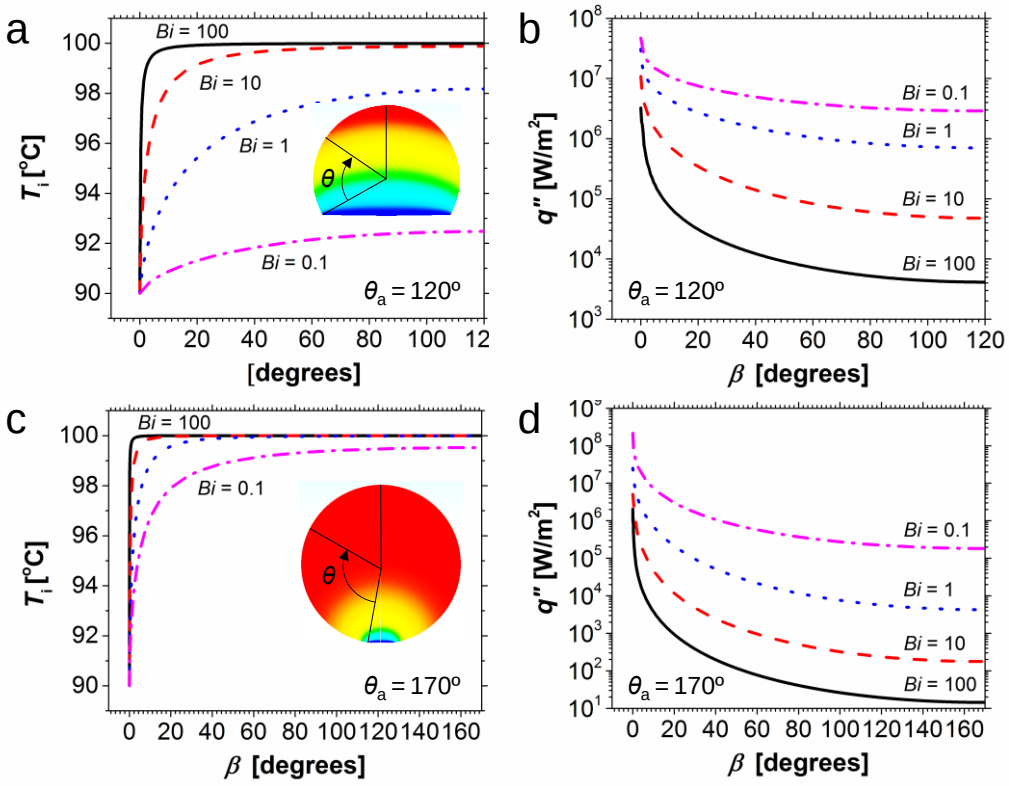

Figure 3.1. (a) Droplet interface temperature (T_i) and (b) local heat flux (q") as a function of interface location (β) for different Biot numbers ($0.1 < Bi < 100$, corresponding to 157 nm < R_b < 157 μm for condensation coefficient, $\alpha = 0.04$), and advancing contact angles (θ_a) of (a-b) 120° and (c-d) 170°. A small condensation coefficient, $\alpha = 0.04$ was used for these simulations in order to obtain larger droplet sizes to more clearly display of gradient of T_i and q" along the condensing interface for a given Bi. Inset of (a) and (c): Droplet cross sectional temperature profile for droplets with $Bi = 0.1$ (droplets not to scale). Small droplets ($Bi \rightarrow 0.1$) with low advancing contact angles ($\theta_a \rightarrow 90°$) have lower temperature gradients at the three phase contact line when compared to large droplets ($Bi \rightarrow 100$) with high advancing contact angles ($\theta_a \rightarrow 180°$). Furthermore, all droplets

show elevated heat flux at the three phase contact line (b, d) due to the low path for heat to travel from the interface to the droplet base, suggesting the importance of understanding local heat transfer in order to obtain high fidelity results.

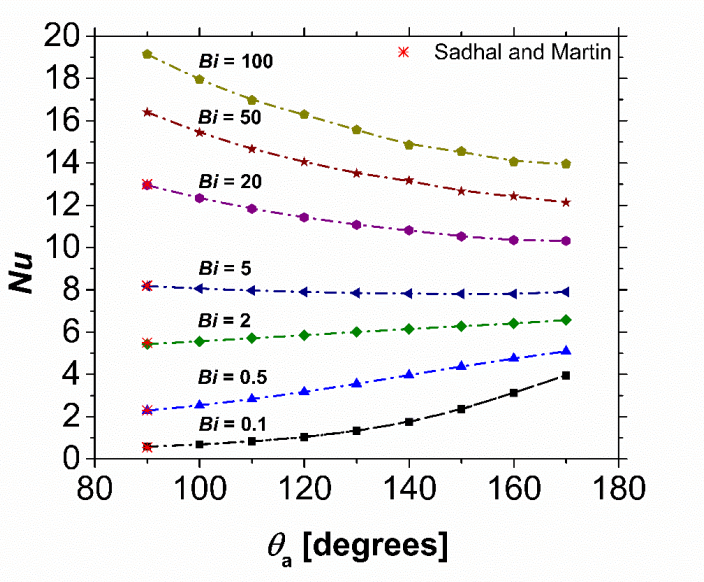

Figure 3.2. Droplet Nusselt number ($Nu = Q/(k_w R_b \Delta T)$) as a function of apparent advancing contact angle (θ_a) for different Biot numbers ($Bi = h_i R_b / k_w$). Small droplets ($Bi < 5$) show an increase in Nu with increased θ_a due to the larger interfacial area for heat transfer. Large droplets ($Bi > 5$) show a decrease in Nu with increased θ_a due to the larger conduction resistance through the droplet. For $Bi \approx 5$, the Nusselt number is approximately constant ($Nu \approx 8$), indicating the droplet size where the interfacial heat transfer resistance is equivalent to the droplet conduction resistance ($R_b \approx 0.16$ μm for $\alpha = 1$). In the limit of $\theta_a = 90°$, exact agreement is observed with previous exact analytical solutions of Sadhal and Martin (red asterisks).[53]

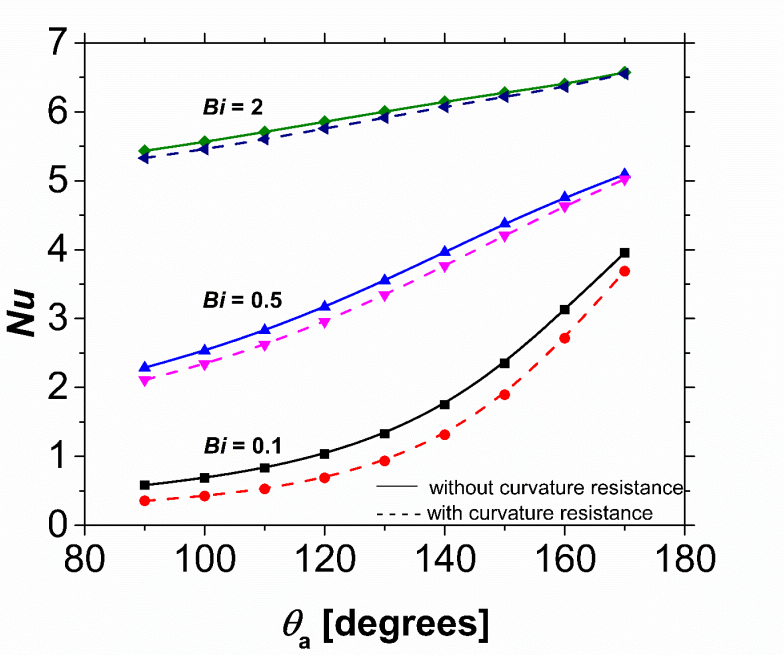

Figure 3.3. Droplet Nusselt number ($Nu = Q/(k_{\mathrm{w}}R_{\mathrm{b}}\Delta T)$) as a function of apparent advancing contact angle (θ_{a}) for different Biot numbers ($Bi = h_{\mathrm{i}}R_{\mathrm{b}}/k_{\mathrm{w}}$) with and without droplet curvature resistance (Kelvin effect). Small droplets ($Bi <$ 5) have higher temperature drop due to higher droplet radius of curvature, $\Delta T_{\mathrm{c}} = 2T_{\mathrm{sat}}\sigma/Rh_{\mathrm{fg}}\rho_{\mathrm{w}}$. At higher Bi ($Bi >$ 5), the curvature resistance becomes negligible due to larger radii of curvature, and hence has little effect on Nu.

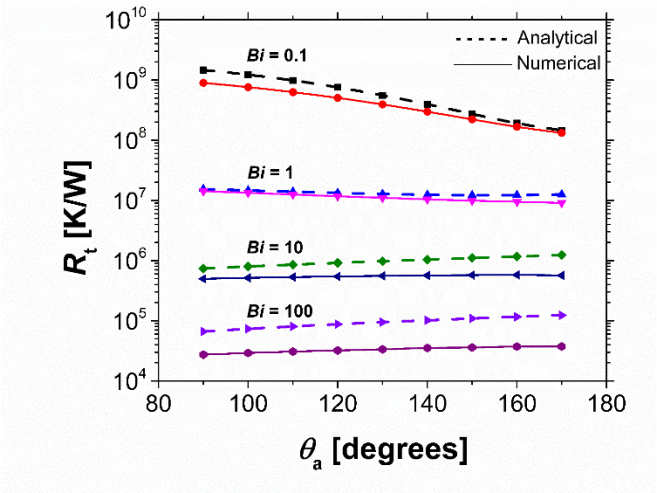

Figure 3.4. Droplet thermal resistance ($R_t = (T_{sat} - T_s)/Q$) as a function of apparent advancing contact angle (θ_a) for different droplet Biot number ($Bi = h_i R_b/k_w$) for condensation coefficient $\alpha = 1$. The thermal resistance is from the vapor (T_{sat}) to the surface (T_s) and combines both the interfacial heat transfer resistance and the conduction resistance through the droplet. The combination of interfacial and conduction resistances was necessary due to the non-uniform free surface temperature (T_i). Both analytical and numerical (our work) values are provided. The analytical solution assumes a constant free-surface temperature with an approximate shape factor to compute the droplet thermal resistance: $R_{t,analytical} = 1/(2\pi R^2 h_i(1 - \cos\theta_a) + \theta_a/(4\pi Rk \sin\theta_a)$.[47] The analytical and numerical results show good agreement for small droplets ($Bi < 5$) due to the negligible droplet conduction resistance in this regime. However, as droplets grow larger ($Bi > 5$), the discrepancy between the numerical and analytical results increases due to the growing influence of droplet conduction on droplet growth and heat transfer.

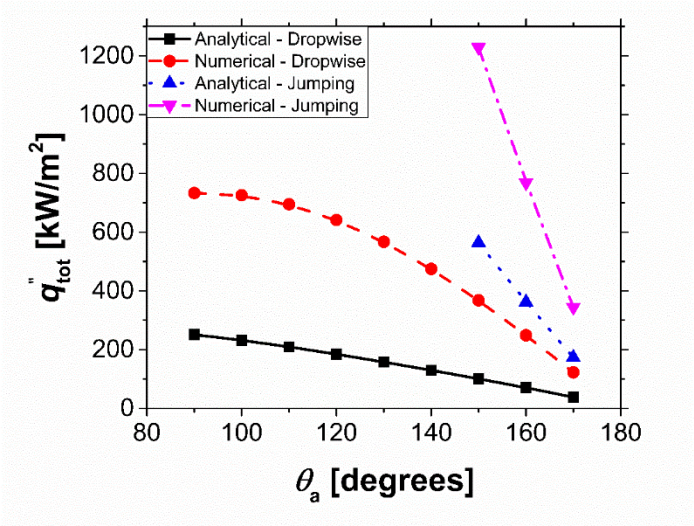

Figure 3.5. Overall steady-state surface heat flux (q") during condensation on a vertical wall as a function of apparent advancing contact angle (θ_a) for dropwise (shedding) and jumping-droplet condensation. For the jumping-droplet solutions, the roughness of surface (r = total area/projected area) was assumed to be 25, corresponding to copper oxide nanostructures. Furthermore, jumping droplet results were only computed for θ_a = 150°, 160° and 170° due to the need for suitably low solid fraction structures with minimal adhesion in order to ensure droplet jumping. The contact angle hysteresis ($\Delta\theta = \theta_a - \theta_r$, where θ_r is the receding contact angle) was assumed to be 10° for dropwise condensation. The results indicate that elevated advancing contact angles lead to degraded performance for both the numerical and analytical solutions due to the elevated droplet conduction resistance. Although higher θ_a leads to smaller droplet departure sizes, the increased droplet thermal resistance outweighs the benefit of smaller droplet distribution. A large discrepancy (≈300%) exists between the numerical and analytical solutions due to the failure of the analytical solution to capture the important heat transfer details at the three phase contact line. Model parameters: condensation coefficient $\alpha = 1$, vapor-to-liquid temperature difference ΔT = 10ºC.

CHAPTER 4: EXPERIMENT SETUP

4.1 Optical Microscopy

4.1.1 Surface Fabrication:

To create the bi-philic sample, commercially available polished multipurpose 110 Cu tabs (25 mm x 2 25 mm x 0.8 mm) were used (99.90% purity), as the test samples for the experiments. Each Cu tab was thoroughly rinsed with acetone, ethanol, isopropyl alcohol (IPA) and deionized (DI) water. The tabs were then dipped into a 5.0 M hydrochloric acid solution for 2 min to remove the native oxide film on the surface, then rinsed with DI water and dried with clean N_2 gas. Nanostructured CuO films were formed by immersing the cleaned tabs into a hot (96 ± 3°C) alkaline solution composed of $NaClO_2$, NaOH, $Na_3PO_4{\cdot}12H_2O$, and DI water (3.75:5:10:100 wt %).[62] To ensure that only one half of each tab be coated with the nanostructure, the tabs were oriented on their sides, and only dipped half way into the alkaline solution (Figure 4.1a). During the oxidation process, a thin (≈300 nm) Cu_2O layer was formed on the dipped side that then re-oxidized to form sharp, knife-like CuO oxide structures with heights of $h \approx 1$ μm (Figure 4.1b). The non-immersed side remained smooth with a gentle tool-finish from sample processing (Figure 4.1c).

4.1.2 Surface Functionalization:

A proprietary fluorinated polymer was deposited using plasma enhanced vapor deposition (P2i). The process occurs under low pressure within a vacuum

chamber at room temperature. The coating is introduced as a vapor and ionized. This process allows for the development of a highly conformal (≈50 nm thick) polymer layer, which forms a covalent bond with the surface (Figure 4.1b).

4.1.3 Surface Characterization:

Contact angle measurements (MCA-3, Kyowa Interface Science Ltd.) of ≈300 nL droplets on a smooth P2i coated silicon wafer showed advancing and receding contact angles of θ_a = 125.4 ± 2.9° and θ_r = 115.1 ± 3.8°, respectively. Using the values of the advancing contact angles on the rough ($\theta_a^{app} \approx 170.5 \pm 7.2°$) and smooth ($\theta_a = 125.4 \pm 2.9°$) P2i surfaces, we estimated the effective solid fraction of the CuO surface to be $\varphi = (\cos\theta_a^{app} + 1)/(\cos\theta_a + 1) \approx 0.04$. The functionalization of the whole surface resulted in ideal bi-philic behavior with the tool-finish hydrophobic (Figure 4.1c) and rough superhydrophobic (Figure 4.1b) regions showing advancing contact angles of $\theta_a \approx 146.0 \pm 2.1°$ and $\theta_a^{app} \approx 170.5 \pm 7.2°$, respectively. Field emission electron micrographs (Hitachi model S-4800) were performed on the sample at an imaging voltage range of 3.0 to 5.0 kV.

4.1.4 Experimental Setup and Procedures:

Droplet growth behavior was studied using a custom built top-view optical light microscopy set-up shown diagrammatically in Figure 4.1d and substantially similar to the one described in Ref.[63] Briefly, samples were placed horizontally on the cold stage (Instec, TP104SC-mK2000A) with a thin film of water underneath in order to provide good thermal communication between the sample and stage.

The cold stage was cooled to the test temperatures of T_s = 10, 5, and 0 ± 0.5°C in a laboratory environment having air temperature, T_{air} = 22 ± 0.5°C, and relative humidity (RH), Φ = 50 ± 1% (Roscid Technologies, RO120). Video recordings were performed at frame rates of 30 frames/s with a high speed camera (Phantom, V711, Vision Research) attached to an upright microscope (Eclipse LV100, Nikon) (Figure 4.1d). Top view imaging was performed with a 20X (TU Plan Fluor EPI, Nikon) objective (Figure 4.1d). For the 20X, lens, the working distance was measured to be 5 ± 0.5 mm. Illumination was supplied by an LED light source (SOLA SM II Light Engine, Lumencor). The LED light source was specifically chosen for its high-intensity and low power consumption (2.5 W) in order to minimize heat generation at the surface due to light absorption and minimize its influence on the droplet growth rates during condensation. Furthermore, by manually reducing the condenser aperture diaphragm opening size and increasing the camera exposure time, we were able to minimize the amount of light energy needed for illumination and hence minimize local heating effects during condensation experiments.[64]

4.2 Environmental Scanning Electron Microscopy

4.2.1 Surface Fabrication:

To create superhydrophobic aluminum oxide samples, the technique given by Ref.[65] was used. Commercially available Al tabs (10mm x 10mm x 0.8 mm) were used (99.90% purity) as the test samples for the experiments. Each Al tab was

ultrasonically treated in acetone and then in ethanol for 5 min. The cleaned samples were dried in a clean N_2 stream. The specimens were then immersed into hot deionized water (90˚C) for one hour, followed by removal and rinsing with room temperature deionized water. This enabled boehmite (Al_2O_3) formation on the Al surface with sharp, knife-like structures having length scales approaching 300 nm.

4.2.2 Surface Functionalization:

Heptadecafluorodecyltrimethoxy-silane (HTMS) was deposited using vapor phase deposition. Nanostructured Al substrates were placed in a container with a vial of 1 mL HTMS toluene solution (5% V). A lid was placed on top to seal the container, followed by heating in an atmospheric pressure oven at 80˚C for 3 hours. This process allows for the development of a highly conformal coating as the HTMS molecules evaporate from solution and re-deposit on the aluminum samples. The same technique was used to coat HTMS on smooth silicon wafers, which were cleaned with acetone, IPA, DI water, and rinsed in clean N_2 prior to functionalization.

4.2.3 Surface Characterization:

Contact angle measurements (MCA-3, Kyowa Interface Science Ltd.) of ≈300 nL droplets on a HTMS coated nanostructured Al surface showed advancing/receding contact angles of $\theta_a^{app}/\theta_r^{app} \approx 170.5 \pm 2.5° / 155 \pm 7°$. Smooth HTMS coated silicon wafers showed advancing/receding contact angles of $\theta_a/\theta_r = 115.5 \pm 4° / 107 \pm 4°$.

4.2.4 Experimental setup and procedure:

To remove the effects of NCGs, we conducted droplet growth experiments in an environmental scanning electron microscope (ESEM; Versa 3D, FEI) that enabled observation of microscale water droplets at saturation vapor pressures of up to 4 kPa ± 0.2%. Prior to the experiments, a Gas Scanning Electron Detector (GSED) and a Peltier stage were mounted inside the ESEM chamber. Each sample substrate was attached to a 5 mm thick copper sample holder with carbon conductive tape and then mounted on the Peltier stage to control the temperature of the sample surface. The chamber was closed and pumped down to high vacuum mode (< 1 mPa) to remove any contaminants or NCGs gas present in the chamber. Prior to condensation, the pressure in the ESEM chamber was maintained at < 100 Pa and the surface temperature was set at 0 ± 0.1°C. To ensure that the surface temperature matches the set temperature, the temperature was maintained for >10 min prior to condensing. Water vapor pressure in the chamber was gradually increased at 50 Pa/min until condensation appeared on the surface at saturation pressures ranging from 630 to 700 Pa. It is important to note, to ensure proper de-gassing of the water vapor supply, which consisted of a Erlenmeyer flask filled with liquid water connected via a software controlled valve, the chamber was cycled from condensation to dry out by initiating condensation at an elevated pressure (typically 1200 ± 2.4 Pa), condensing for a full 2 minutes, re-heating the stage to evaporate the condensed water, and pumping down to 50 ± 0.1Pa to remove the evaporated vapor. By cycling the evaporation/pump-down cycle 10 times, we

ensure that any NCG content in the vapor supply line has been removed and pumped out of the system. To avoid droplet evaporation as a result of heating by the electron beam, the voltage and current of the electron beam were set at 10 kV and < 12pA, respectively. Droplet growth videos were captured at approximately one frame (768 by 556 pixels) every 2 seconds (dwell time per pixel ~3 μs).

4.3 Figures

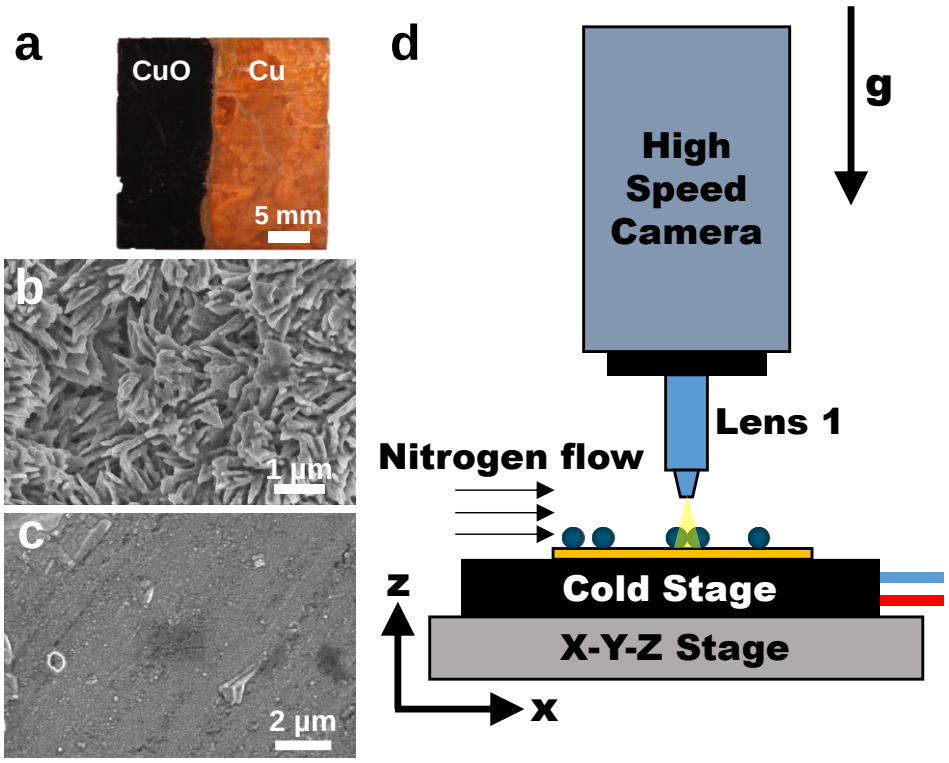

Figure 4.1. (a) Top view image of the bi-philic sample with tool-finish hydrophobic (orange) and rough superhydrophobic (black) regions. Field emission scanning electron micrographs of (b) a 10 min oxidized nanostructured CuO surface coated with a ≈ 50 nm thick layer of P2i fluoropolymer and (c) tool-finish Cu surface coated with a ≈ 50 nm thick layer of P2i fluoropolymer. The sharp, knife-like CuO structures have characteristic heights, $h \approx 1$ μm, and solid fraction, $\varphi \approx 0.04$. The macroscopically measured advancing apparent contact angle on the tool-

finish hydrophobic Cu and superhydrophobic CuO surfaces was $\theta_a{}^{app} \approx 146.0 \pm 2.1°$ and $\theta_a{}^{app} \approx 170.5 \pm 7.2°$, respectively. (d) Schematic of the optical microscopy experimental setup used to study the growth rate of condensing water droplets. Droplet growth movies were recorded at 30 frames per second. Experimental conditions: stage and sample temperature T_s = 10, 5, and 0 ± 0.5°C, ambient air temperature T_{air} = 22 ± 0.5°C, vapor temperature $T_v = T_{sat}\left(\Phi P_{sat}(T_{air})\right)$ = 11.1 ± 0.5°C, relative humidity Φ = 50 ± 1%, and supersaturation $S = [\Phi P_{sat}(T_{air})]/ P_{sat}(T_w)$ = 1.07 ± 0.035, 1.51 ± 0.052, 2.16 ± 0.085. The relative humidity of the laboratory air could vary up to ± 10% over the course of a day. To ensure stable humidity conditions, the experiments were conducted in hour-long segments when Φ reached 50%, and ended when Φ exceeded 52% or fell below 48%. Schematics not to scale.

CHAPTER 5: EXPERIMENTS

5.1 Optical Microscopy

In order to verify the numerical results and compare them to the SoA analytical model, [47] we conducted droplet growth experiments on a bi-philic surface composed of a smooth hydrophobic finish on one half, and a rough nanoscale superhydrophobic coating on the other (Figure 4.1a). We chose to work with a single bi-philic sample instead of two separate samples having distinct wettability in order to ensure identical local droplet growth conditions (local wall temperature and vapor pressure) in the viewing microscopy area (~ 100 μm^2). By observing and measuring the droplet growth rate at the interface between the two regions of differing wettability, we were able to capture droplet growth on both hydrophobic and superhydrophobic regions and ensure that the local supersaturation is the same. Furthermore, the use of a single bi-philic sample resulted in identical parasitic thermal resistances, such as mounting thermal grease uniformity and sample thickness, for all droplets being measured.

Figure 5.1a and b show time lapse images of individual droplet growth on the superhydrophobic and hydrophobic regions, respectively, which highlights the relatively similar growth rates on the two surfaces. As the droplets grew and began to interact with each other on the superhydrophobic regions, removal via coalescence-induced droplet ejection was observed.[14] Indeed, the sharp knife-like roughness features of the CuO structure act to both minimize the contact line

pinning force, and ensure the formation of partially wetting droplets, ideal for enhanced condensation heat transfer.[61] To quantify the growth dynamics, we examined the time lapse images to obtain the average droplet diameter ($\langle D \rangle$) as a function of time (t) for the superhydrophobic (Figure 5.1c) and hydrophobic (Figure 5.1d) areas. The initial growth rate of droplets on the superhydrophobic surface ($d\langle D \rangle/dt$ = 0.2 μm/s) was ≈1.5X lower than that of the hydrophobic surface ($d\langle D \rangle/dt$ = 0.3 μm/s) for $\langle D \rangle$ < 12 μm. As the droplets reached diameters $\langle D \rangle$ > 15 μm, the growth rates discrepancy decreased, with the superhydrophobic droplet growth rate ($d\langle D \rangle/dt$ = 0.05 μm/s) approaching the hydrophobic droplet growth rate ($d\langle D \rangle/dt$ = 0.1 μm/s).

To provide insight into the experimental results, capture the growth dynamics related to the different droplet morphologies, and verify the numerical simulation results, we modeled the experimental droplet growth behavior with our developed simulations and an SoA analytical model.[47] To determine the theoretical growth rate ($dD/dt = 2dR/dt$), the individual droplet heat transfer $Q(R, \theta)$ is related to the droplet growth rate by the latent heat of phase change[39]

$$\begin{aligned} Q(R,\theta) = \dot{m} h_{fg} &= \rho_w h_{fg} \frac{dV}{dt} \\ &= \frac{\pi}{3} \rho_w h_{fg} \frac{d}{dt} [(1-\cos\theta)^2 (2+\cos\theta) R^3] \,. \end{aligned} \tag{5.1}$$

Differentiating Equation (5.1), we obtain explicit term for dR/dt

$$Q(R,\theta) = \pi\rho_w h_{fg} R^2 \frac{dR}{dt}\left\{(1-\cos^2\theta)^2 \sin\theta \frac{d\theta}{dR} R + (1-\cos\theta)^2(2 + \cos\theta)\right\}. \quad (5.2)$$

The individual droplet heat transfer, $Q(R,\theta) = f(T_s, \alpha, P_{sat})$, was computed using our simulation (black solid line) and the SoA analytical model (blue dotted line). When a water droplet nucleates and grows on the superhydrophobic surface, a varying contact angle is observed initially (D < 6-8 μm) because of locally pinned contact lines at droplet base.[36] Thus, in order to simulate the growth of droplets on the superhydrophobic surface (Figure 5.1a), we used a band approximation for the advancing contact angle, with θ_a = 150° for $D \leq$ 7 μm, θ_a = 160° for 7 μm$< D \leq$ 14 μm and θ_a = 170° for $D >$ 14 μm, in agreement with previous well characterized droplet growth studies during condensation on superhydrophobic CuO.[36] For droplet growing on the hydrophobic surface, droplet contact angle variation as a function of droplet diameter was not observed, thus a constant θ_a = 140° was used for the models.

The results of the numerical model are shown in Figure 5.1c and d, and is in excellent agreement with the experiments (red circles). The analytical model, however, tended to underestimate the experimental growth rate due to the lack of taking into account local heat transfer effects at the three phase contact line. As observed in the experiments, the numerical model shows that for large droplet diameters (D > 15 μm), droplets growing on the superhydrophobic surface have

slightly lower growth rates than droplet on the hydrophobic surface due to the added conduction thermal resistance. While at low droplet diameters (D < 15 μm), the growth rate of the superhydrophobic droplets is faster due to interfacial thermal resistance dominated growth. The model solutions were obtained for surface-to-vapor temperature difference $\Delta T_{\text{numerical}} = \Delta T_{\text{analytical}}$ = 0.0018°C, where ΔT was chosen based on the best fit between the numerical model and experimental growth rate data. The experimental surface-to-vapor temperature difference, $\Delta T_{\text{exp}} = T_{\text{sat}}\left(\Phi P_{\text{sat}}(T_{\text{air}})\right) - T_{\text{s}}$ = 6.1 ± 0.58°C, was three orders of magnitude larger than the numerical temperature difference. The significant discrepancy between model and experiment can be attributed to the presence of non-condensable gases (NCGs). The condensation of water vapor acts to leave behind NCGs (air) that blanket the surface and act as a diffusion barrier for water vapor.[66, 67] The counter diffusion of water vapor to the surface, coupled with the diffusion of NCGs away from the surface, acts to significantly deteriorate the condensation heat transfer process, and hence decrease the effective surface-to-vapor temperature difference. Interestingly, previous analysis of filmwise condensation in the presence of NCGs showed temperature drops of similar orders of magnitude as observed in these experiments, with ~2°C happening in the vapor diffusion layer, and ~0.01°C occurring in the condensate film.[68]

As a secondary artifact, the presence of NCGs can be observed through the relatively large error bars in the droplet growth data (Figure 5.1c and d). Significant

variability in individual droplet growth was observed based on the location of droplets relative to one another, with isolated droplets growing faster than droplet residing close to many neighbors. The droplet growth variability can also be attributed to the presence of NCGs, formation of vapor depletion layers and concentration boundary layer overlap from droplet-to-droplet.[69-71]

In order to gain further insight, we compared the experimental results with the power law exponent model.[71] When droplet dimensions are larger than the surface pattern length scales ($\langle D \rangle$ > 1 μm, as observed here), droplets grow as breath figures on a surface with an expected average droplet diameter of $\langle D \rangle = At^{\mu}$, where μ, the power law exponent, ranges from 0 to 1 depending on the droplet, substrate dimensions, and growth limiting conditions. In these experiments, due to the presences of NCGs, we expect vapor diffusion limitations to be dominate droplet growth dynamics.

As the droplet grows, direct accommodation of water molecules at liquid-vapor interface establishes a 3D concentration gradient of water molecules inside the vapor surrounding the droplet. For a constant flux of water molecules hitting the water droplet surface, the concentration gradient should vary as $1/R^2$, where R is the radius of the water droplet, resulting in a scaled droplet volumetric growth rate of:

$$\frac{dV}{dt} \sim 4\pi R^2 \frac{dR}{dt} \sim 4\pi R^2 \left(\frac{1}{R^2}\right) D_{12} \tag{5.3}$$

where, V is the volume of water droplet, D_{12} is mutual diffusion coefficient of water in air. Rearranging Equation 13 reveals: $D \sim t^{1/3}$ (μ = 0.3) at short timescales immediately after nucleation when local vapor concentration boundary layers surrounding individual droplets do not interact with one another (vapor depletion layers).

At later times, after vapor diffusion boundary layers begin to overlap, the concentration of water vapor molecules can be assumed to be constant only in a region far from the surface, resulting in a concentration gradient that varies as $1/R$. Thus, scaling analysis yields:

$$\frac{dV}{dt} \sim 4\pi R^2 \frac{dR}{dt} \sim 4\pi R^2 \left(\frac{1}{R}\right) D_{12} \tag{5.4}$$

Rearranging Equation 5.4 reveals: $D \sim t^{1/2}$ (μ = 0.5) at longer timescales when overlapping diffusion boundary layers dominate and a macroscale NCG layer blankets the surface.

Interestingly, the experimental results of Figures 8c and d agree remarkably well with the scaling analysis, revealing that the droplet power law is obeyed by both superhydrophobic and hydrophobic surfaces with μ_{SHP} = 0.3, μ_H = 0.2 at early timescales when local vapor diffusion barriers dominate, and μ_{SHP} = μ_H = 0.5 at

later timescales. The power law results reinforce the critical importance that NCGs play in the dynamics of droplet growth and help clarify the remarkably similar growth rates and low model temperature differences needed to match the simulations to the experiments.

Fitting of ΔT for the other experimental cases having T_s = 10, 5, and 0ºC yielded ΔT = 0.0015, 0.0018, and 0.0025 ºC, respectively, in agreement with the fact that NCGs act to dominate the vapor and heat transport in these experiments. It is important to note that for all experiments, fitting with the same value of ΔT for both superhydrophobic and hydrophobic droplet growth yielded the best numerical model fit to the experimental results. The good agreement is due to our experimental ability to maintain the same local conditions (supersaturation) for both surfaces via the bi-philic surface design.

Perhaps the most interesting aspect of the optical microscopy studies, in addition to their ability to validate the numerical simulations, is that droplet jumping was observed on the superhydrophobic area for all macroscopically measured supersaturations, $S = [\Phi P_{\mathrm{sat}}(T_{\mathrm{air}})]/P_{\mathrm{sat}}(T_{\mathrm{s}})$ = 1.07 ± 0.035, 1.51 ± 0.052, and 2.16 ± 0.085. Contrary to previous studies on superhydrophobic CuO,[61] nucleation mediated flooding due to saturation of nucleation sites on the surface at S > 1.2 was not observed in these experiments. The reason for the elevated critical supersaturation is attributed to the presence of NCGs, which were not present in previous studies. The results shown here point to the need to classify

nucleation mediated flooding based on surface heat flux (q_{cr}" > 8 W/cm^2) as opposed to the critical supersaturation ($S_{cr} \approx 1.12$), as identical macroscopic supersaturations in pure vapor environments and NCG environments yield strikingly different condensation, nucleation, and heat flux behavior.

5.2 Environmental Scanning Electron Microscopy

To remove the effects of NCGs, we conducted droplet growth experiments in an environmental scanning electron microscope (ESEM) that enabled observation of microscale water droplets at saturation vapor pressures of up to 4 kPa ± 0.2%. The removal of NCGs eliminated the dominant vapor diffusion resistance (not accounted for in the numerical or analytical model), enabled the principal thermal resistances governing droplet growth to come into play, and hence validate our model with higher accuracy.

For the ESEM experiments, boehmite nanostructures on aluminum and smooth silicon wafers functionalized with hydrophobic self-assembled monolayers of HTMS were used to obtain superhydrophobic and hydrophobic droplet morphologies, respectively. The change from copper (~800 nm) to aluminum based nanostructures (~300 nm) does not alter the growth dynamics of condensing droplets due to the negligible thermal resistance of the partially wetted base for both surfaces. Furthermore, smooth silicon was used instead of tool finish copper due to our desire to observe droplet growth behavior on lower advancing contact angle surfaces to investigate the robustness of our numerical model.

Figure 5.2a and b show ESEM time lapse images of individual droplet growth on the superhydrophobic nanostructured aluminum surface and hydrophobic smooth silicon surface, which highlights the difference in droplet growth rate. Droplet growth on the surfaces was characterized at a water vapor pressure P_v = 700 ± 1.4Pa, corresponding to a saturation temperature of 1.9 ± 0.004ºC, and substrate temperature T_s = 1.8 ± 0.1ºC. The experimentally obtained droplet diameter as a function of time for superhydrophobic and hydrophobic morphologies are shown in Figure 5.2c and d respectively. Scatter in the droplet growth data was almost nonexistent, with droplets growing, coalescing, jumping, and re-growing in a self-similar manner for each cycle. In addition, the droplet growth rate of adjacent droplets was also identical in nature. The lower variability in growth rate is attributed to the lack of NCGs in the ESEM environment. The vapor diffusion resistance is much smaller, and hence, droplet growth dynamics are limited mainly by interfacial resistance at early times, and conduction resistance at later times.

To provide insight into the ESEM results and verify our simulations, we modeled the experimental droplet growth behavior with the numerical and analytical models according to Equation (12). The results of the numerical model are shown in Figure 5.2c and d, and are in excellent agreement with the experiments. The removal of NCGs acted to accentuate the growth rate difference between the two droplet morphologies. As observed in the experiments, the numerical model shows that for large diameters (D > 20 μm), droplets growing on

the superhydrophobic surface have lower growth rates ($d\langle D\rangle/dt$ = 0.06 μm/s) than droplet on the hydrophobic surface ($d\langle D\rangle/dt$ = 0.2 μm/s) due to the added conduction thermal resistance. While at low diameters (D < 20 μm), the growth rate of the superhydrophobic droplets ($d\langle D\rangle/dt$ = 1.0 μm/s) is much faster due to interfacial thermal resistance dominated growth. These same trends were observed in the optical microscopy results, however with lower growth rate difference between the two droplet morphologies arising from 1) the higher advancing contact angle of the tool-finish copper surface, and 2) the removal of the external vapor diffusion resistance, which acted to minimize growth differences due to morphology. The ESEM model solutions were obtained for surface-to-vapor temperature difference $\Delta T_{\text{numerical}} = \Delta T_{\text{analytical}}$ = 0.01°C, where ΔT was chosen based on the best fit between the numerical model and experimental growth rate data. The experimental surface-to-vapor temperature difference, $\Delta T_{\text{exp}} = T_{\text{v}} - T_{\text{s}}$ = 0.1 ± 0.1°C, was in excellent agreement with the numerical temperature difference. The value used in the numerical model is within the error of the experimental apparatus.

It is important to note that for the smooth hydrophobic silicon surface (Figure 5.2b and d), the ESEM model solutions were obtained for surface-to-vapor temperature difference ΔT = 0.004°C, which was different from the superhydrophobic solution (ΔT = 0.01°C), and within the error of the experimental apparatus. The model ΔT values for superhydrophobic and hydrophobic surfaces

did not match because the experiments were not done at the same time. Unlike the optical microscopy experiments, where bi-philic samples were used and observed simultaneously, the ESEM results were obtained with different samples and individual runs for each sample, leading to different local supersaturations depending on the viewing location, viewing angle, and beam conditions, and hence different ΔT.

Analysis of the droplet growth using scaling arguments and the power law growth model revealed excellent agreement between theory and observations. For the ESEM experiments, growth of larger droplets (D > 20 μm) is limited by conduction resistance, which can be estimated analytically to approach $\approx 4\pi R k_w \sin\theta_a / \theta_a$.[39, 47] Scaling of the droplet growth rate with conduction heat transfer through the droplet, we obtain:

$$\frac{dV}{dt} \sim 4\pi R^2 \frac{dR}{dt} \sim \pi R^2 \left(\frac{4k_w \sin\theta_a}{R\theta_a}\right) \tag{5.5}$$

Rearranging Equation 5.5 reveals: $D \sim t^{1/2}$ (μ = 0.5) at longer timescales when droplet conduction dominates. While the power law exponent at large droplet sizes is identical for the optical microscopy and ESEM experiments, the mechanisms of growth are drastically different.

At low droplet diameters (D < 20 μm), we expect the ESEM droplet growth to be limited by vapor molecule accommodation and the liquid-vapor interfacial

heat transfer resistance ($\sim 1/4\pi R^2 h_{\mathrm{i}}$). Scaling of the droplet growth rate with convection at the liquid vapor interface, we obtain:

$$\frac{dV}{dt} \sim 4\pi R^2 \frac{dR}{dt} \sim 4\pi R^2 h_{\mathrm{i}} \tag{5.6}$$

Rearranging Equation 5.6 reveals: $D \sim t^1$ (μ = 1) at short timescales.

Figures 5.2c and d reveal that while the simplistic power law model agreed well with the experimental results for large conduction limited droplets ($\mu_{SHP} = \mu_H$ = 0.5), it failed to quantitatively capture the droplet growth at small scales where the simulations predict convection to dominate. The discrepancy between power law model and ESEM experiments can be explained by two potential mechanisms: 1) higher sensitivity to electron beam heating at low droplet diameters, or 2) surface diffusion limited growth.[69, 71] Indeed, both mechanisms will act to decrease the droplet growth rate. Although surface diffusion of water clusters to the droplet contact line yield a droplet growth dependence of: $D \sim t^{1/3}$ (μ = 1/3) at short timescales, it is an unlikely mechanism governing growth at the observed length scales (> 1μm).[72-74] Hence, electron beam heating is the likely reason for reduced droplet growth as even very small electron beam powers can alter the growth dynamics for small (R < 5μm) droplets.

The droplet growth experiments shown here not only validate the developed numerical model of condensation on hydrophobic and superhydrophobic surfaces,

they reinforce the picture that future high fidelity studies of droplet growth must take into account the NCG content of the saturated vapor. While the effects of NCGs was mitigated here by the use of ESEM microscopy, more work is needed to study the effects of NCGs on droplet nucleation and nucleation-mediated flooding on superhydrophobic surfaces. Although our model and experimental results represent a clearer physical picture of condensate droplet growth, the assumption of constant far field vapor temperature (T_v) are yet to be validated. Superhydrophobic surfaces undergoing condensation form a high density of very spherical droplets, resulting in vapor molecule scattering, ballistic vapor transport effects, and non-classical effects governing access of vapor molecules to the liquid-vapor interface beneath high contact angle droplets.[75] Future investigation of droplet nucleation and growth of droplet residing in the vapor wedge beneath large droplets are needed in order to understand these non-classical effects.

The simulation and results presented here are analogous to those done for the study of evaporation heat transfer on hydrophilic substrates.[76-78] Like evaporation, our results demonstrate the importance of analyzing local heat transfer effects at the three phase contact line in order to obtain high fidelity results for condensation on both hydrophobic and superhydrophobic surfaces. In the future, it would be interesting to extend the present model to be able to consider the composite thermal resistance (vapor/liquid gap) beneath the droplet commonly seen on Cassie-stable microstructured superhydrophobic surfaces features.[37] In addition, the use of constant contact angle droplet growth may not be valid for

microstructured superhydrophobic surfaces, pointing to a need to incorporate the microstructure in the numerical simulations along with radius dependent advancing contact angle instead of the band approximation used here.[79] Furthermore, it would be interesting to incorporate effects of Marangoni convection for droplets with larger radii ($Bi > 10^4$ for condensation coefficient, $\alpha = 1$), where Marangoni forces become significant, to study the effects of enhanced internal droplet heat transfer.

5.3 Figures

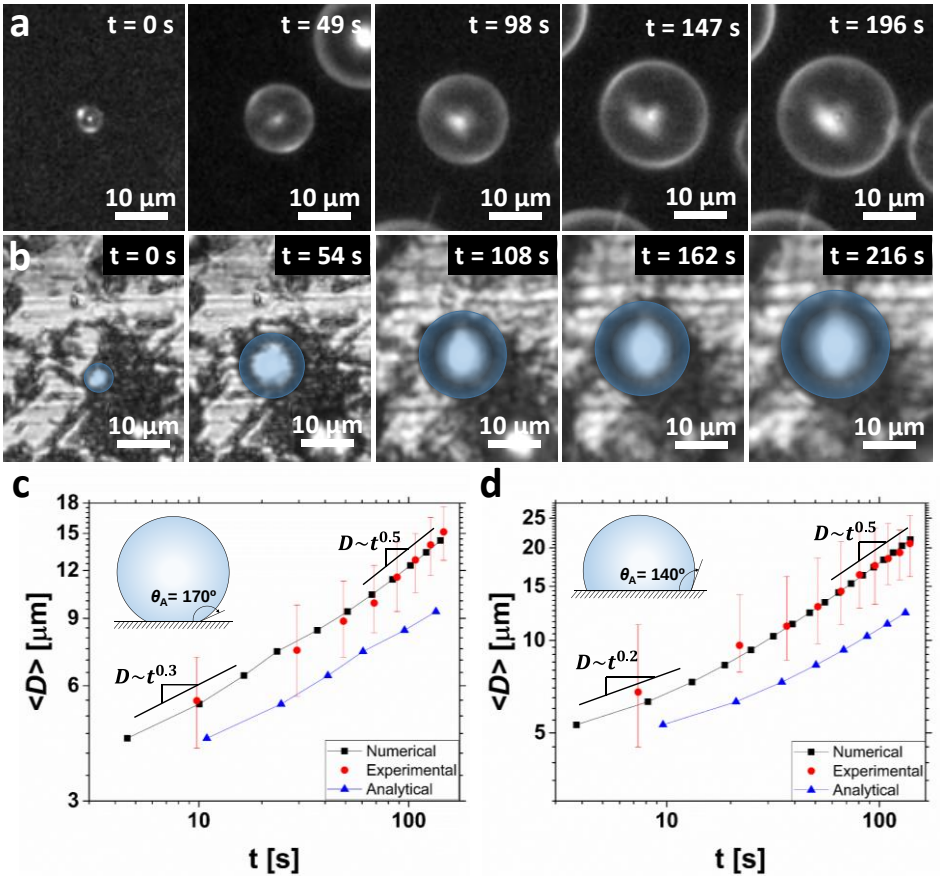

Figure 5.1. Time lapse optical microscopy images of droplet growth during water vapor condensation on the (a) superhydrophobic region ($\theta_a^{app} \approx 170.5 \pm 7.2°$) and hydrophobic region ($\theta_a^{app} \approx 146.0 \pm 2.1°$) of the bi-philic sample (Figure 4.1a). The droplet growing on the hydrophobic region (b) has been false-colored blue for clarity. The bi-philic surface was maintained at 5°C prior to condensation initiation. Time evolution of the average droplet diameter ($\langle D \rangle$) on the (c) superhydrophobic and (d) hydrophobic regions. At early stages ($\langle D \rangle$ < 15 µm), rapid growth of superhydrophobic droplets results due to low conduction resistance through the droplet and high interfacial area. Inset: Schematic of the droplet morphology. At later stages ($\langle D \rangle$ > 15 µm), the superhydrophobic and hydrophobic growth rates converge due to the dominant conduction thermal resistance of the droplet. The

presence of NCGs acts to decrease the effects of droplet heat transfer physics, and dominates the thermal resistance of the droplet growth by placing more emphasis on the external vapor diffusion resistance. For the analytical and numerical models, the vapor-to-surface temperature difference $\Delta T = 0.0018°C$ was used to fit the experimental data.

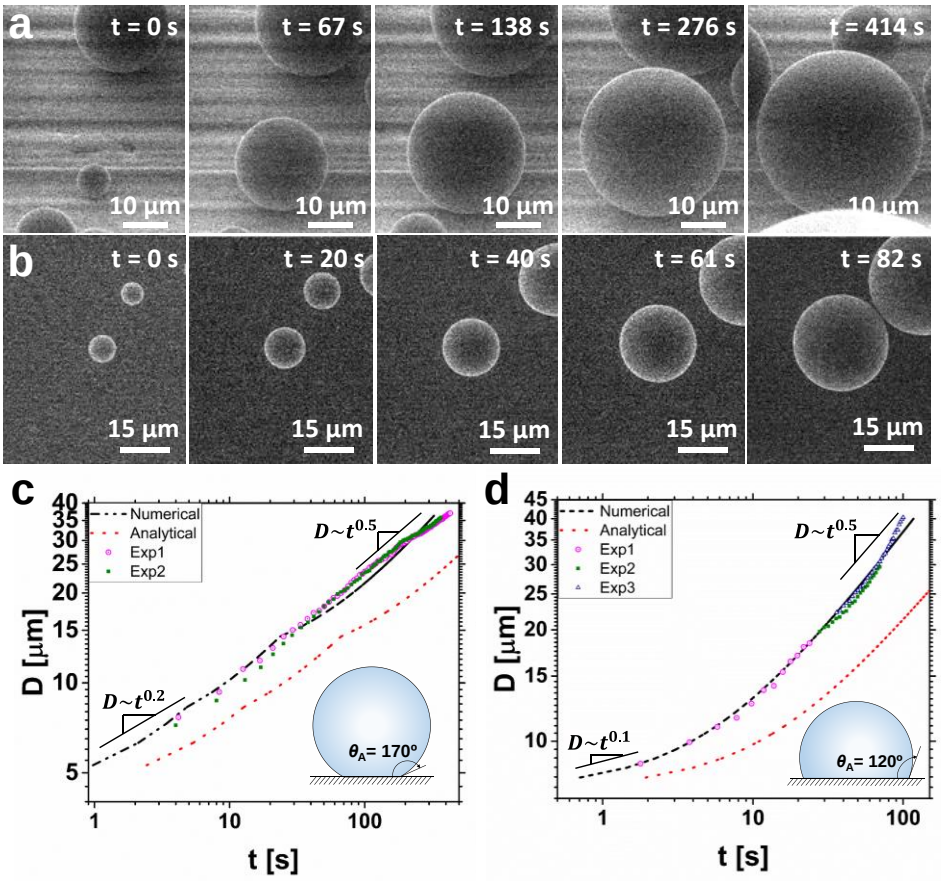

Figure 5.2. Time lapse ESEM images of droplet growth during saturated water vapor condensation on the (a) superhydrophobic Al ($\theta_a{}^{app} \approx 170.5 \pm 2.5°$) and (b) smooth hydrophobic SiO_2 ($\theta_a \approx 125.4 \pm 2.9°$) samples, respectively. Time evolution of the average droplet diameter ($\langle D \rangle$) on the (c) superhydrophobic and (d) hydrophobic samples. Inset: Schematic of the droplet morphology. The elimination of NCGs from the water vapor amplified the effects of interfacial and

droplet conduction resistances. At later stages of growth ($\langle D \rangle$ > 20 μm), the hydrophobic droplet growth rate is much faster than the superhydrophobic due to reduced droplet conduction resistance. For the analytical and numerical models, a vapor-to-surface temperature difference of $\Delta T_{numerical} = 0.01°C$ was used to fit the experimental data. The experimental surface-to-vapor temperature difference, $\Delta T_{\mathrm{exp}} = T_{\mathrm{v}} - T_{\mathrm{s}}$ = 0.1 ± 0.1°C, was in excellent agreement with the numerical temperature difference and within the error of the experimental apparatus. The removal of NCGs eliminated the dominant vapor diffusion resistance (not accounted for in the numerical or analytical model), enabled the principal thermal resistances governing droplet growth to come into play, and hence validate our model with higher accuracy.

CHAPTER 6: CONCLUSIONS

In summary, we developed a 2D axisymmetric numerical simulation of individual droplet heat transfer valid for both hydrophobic and superhydrophobic surfaces undergoing dropwise and jumping-droplet condensation. Unlike previous works, which utilize constant temperature boundary conditions and shape factor approximations, our work resolves the full droplet temperature and heat flux distribution, showing that the interfacial temperature does indeed vary at the free surface, and that local heat transfer at the three phase contact line can be 4 orders of magnitude higher when compared to the droplet top. We computed the droplet Nusselt number and effective thermal resistance, showing discrepancies between our results and the previous models at higher droplet radii due to the elevated droplet conduction resistance. Through the integration of our model results and droplet distribution theory, we demonstrated that the currently accepted shape-factor based analytical models tend to underestimate heat transfer by as much as 300%, due to their inability to resolve heat transport at the three phase contact line. To validate our developed model, we conducted optical and environmental scanning electron microscopy in humid air and pure saturated water vapor environments, respectively. The experimental results not only validated out model predictions, but quantified the detrimental effects of non-condensable gases on droplet growth. These results shed light on the previously unidentified importance of the droplet three phase contact line for dropwise and jumping-droplet condensation heat and mass transfer on hydrophobic and nanostructured

superhydrophobic surfaces, respectively. Furthermore, the results provide a simulation framework to further study and resolve local heat transfer effects for various phase change applications such as droplet evaporation and freezing where analogous heat transfer processes through individual droplets take place for energy and water applications.

REFERENCES

[1] L. Perez-Lombard, J. Ortiz, C. Pout, Energ Buildings 2008, 40, 394.

[2] B. Z. Li, R. M. Yao, Renew Energ 2009, 34, 1994.

[3] M. H. Kim, C. W. Bullard, Int J Refrig 2002, 25, 924.

[4] J. M. Beer, Prog Energ Combust 2007, 33, 107.

[5] T. B. Peters, M. McCarthy, J. Allison, F. A. Dominguez-Espinosa, D. Jenicek, H. A. Kariya, W. L. Staats, J. G. Brisson, J. H. Lang, E. N. Wang, Ieee T Comp Pack Man 2012, 2, 1637.

[6] E. J. Le Fevre, J. W. Rose, International Journal of Heat and Mass Transfer 1964, 7, 272.

[7] E. J. Le Fevre, J. W. Rose, "A Theory af Heat Transfer by Dropwise Condensation", presented at *Proceedings of the Third International Heat Transfer Conference*, Chicago, IL, 1966.

[8] B. B. Mikic, International Journal of Heat and Mass Transfer 1969, 12, 1311.

[9] J. W. Rose, International Journal of Heat and Mass Transfer 1967, 10, 755.

[10] J. W. Rose, P I Mech Eng a-J Pow 2002, 216, 115.

[11] E. Schmidt, W. Schurig, W. Sellschopp, Forsch. Ingenieurwes 1930, 1, 53.

[12] A. Lafuma, D. Quere, Nat Mater 2003, 2, 457.

[13] D. Quere, Annu Rev Mater Res 2008, 38, 71.

[14] J. B. Boreyko, C. H. Chen, Phys Rev Lett 2009, 103, 184501.

[15] R. Enright, N. Miljkovic, J. Sprittles, K. Nolan, R. Mitchell, E. N. Wang, ACS Nano 2014, 8, 10352.

[16] F. J. Liu, G. Ghigliotti, J. J. Feng, C. H. Chen, J Fluid Mech 2014, 752, 39.

[17] F. J. Liu, G. Ghigliotti, J. J. Feng, C. H. Chen, J Fluid Mech 2014, 752, 22.

[18] Y. Nam, H. Kim, S. Shin, Appl Phys Lett 2013, 103.

[19] Y. Nam, D. Seo, C. Lee, S. Shin, Soft Matter 2015, 11, 154.

[20] N. Miljkovic, R. Enright, Y. Nam, K. Lopez, N. Dou, J. Sack, E. N. Wang, Nano Letters 2013, 13, 179.

[21] K. Rykaczewski, W. A. Osborn, J. Chinn, M. L. Walker, J. H. J. Scott, W. Jones, C. Hao, S. Yaod, Z. Wang, Soft Matter 2012, 8, 8786.

[22] K. M. Wisdom, J. A. Watson, X. Qua, F. Liua, G. S. Watson, C. H. Chen, Proceedings of the National Academy of Sciences of the United States of America 2013, 110, 7992.

[23] G. S. Watson, L. Schwarzkopf, B. W. Cribb, S. Myhra, M. Gellender, J. A. Watson, J R Soc Interface 2015, 12.

[24] G. S. Watson, M. Gellender, J. A. Watson, Biofouling 2014, 30, 427.

[25] J. B. Boreyko, Y. J. Zhao, C. H. Chen, Appl Phys Lett 2011, 99, 234105.

[26] J. B. Boreyko, P. C. Collier, Acs Nano 2013, 7, 1618.

[27] X. M. Chen, R. Y. Ma, H. B. Zhou, X. F. Zhou, L. F. Che, S. H. Yao, Z. K. Wang, Sci Rep-Uk 2013, 3.

[28] J. Y. Lv, Y. L. Song, L. Jiang, J. J. Wang, ACS Nano 2014, 8, 3152.

[29] Q. L. Zhang, M. He, J. Chen, J. J. Wang, Y. L. Song, L. Jiang, Chem Commun 2013, 49, 4516.

[30] J. B. Boreyko, C. H. Chen, International Journal of Heat and Mass Transfer 2013, 61, 409.

[31] D. J. Preston, N. Miljkovic, R. Enright, E. N. Wang, J Heat Trans-T Asme 2014, 136.

[32] N. Miljkovic, D. J. Preston, R. Enright, E. N. Wang, Appl Phys Lett 2014, 105.

[33] N. Miljkovic, D. J. Preston, R. Enright, E. N. Wang, Nat Commun 2013, 4.

[34] R. Enright, N. Miljkovic, J. L. Alvarado, K. Kim, J. W. Rose, Nanosc Microsc Therm 2014, 18, 223.

[35] N. Miljkovic, E. N. Wang, Mrs Bull 2013, 38, 397.

[36] R. Enright, N. Miljkovic, N. Dou, Y. Nam, E. N. Wang, J Heat Transf 2013, 135, 091304.

[37] N. Miljkovic, R. Enright, E. N. Wang, Acs Nano 2012, 6, 1776.

[38] N. Miljkovic, R. Enright, E. N. Wang, 3rd Micro/Nanoscale Heat & Mass Transfer International Conference 2012.

[39] N. Miljkovic, R. Enright, E. N. Wang, J Heat Transf 2013, 135.

[40] J. Cheng, A. Vandadi, C. L. Chen, Appl Phys Lett 2012, 101, 131909.

[41] E. Olceroglu, C. Y. Hsieh, M. M. Rahman, K. K. S. Lau, M. McCarthy, Langmuir 2014, 30, 7556.

[42] E. Olceroglu, S. M. King, M. M. Rahman, M. McCarthy, Proceedings of the Asme International Mechanical Engineering Congress and Exposition - 2012, Vol 7, Pts a-D 2013, 2809.

[43] D. Attinger, C. Frankiewicz, A. R. Betz, T. M. Schutzius, R. Ganguly, A. Das, C.-J. Kim, C. M. Megaridis, MRS Energy & Sustainability 2014, 1.

[44] X. M. Chen, J. A. Weibel, S. V. Garimella, Adv Mater Interfaces 2015, 2.

[45] Y. M. Hou, M. Yu, X. M. Chen, Z. K. Wang, S. H. Yao, ACS Nano 2015, 9, 71.

[46] H. Kim, Y. Nam, International Journal of Heat and Mass Transfer 2016, 93, 286.

[47] S. Kim, K. J. Kim, J Heat Transf 2011, 133, 081502.

[48] J. W. Rose, International Journal of Heat and Mass Transfer 1972, 15, 1431.

[49] N. Fatica, D. L. Katz, Chem Eng Prog 1949, 45, 661.

[50] J. L. McCormick, E. Baer, J Coll Sci Imp U Tok 1963, 18, 208.

[51] B. T. Nijaguna, Appl Sci Res 1974, 29, 226.

[52] A. Umur, P. Griffith, J Heat Transf 1965, 87, 275.

[53] S. S. Sadhal, W. W. Martin, International Journal of Heat and Mass Transfer 1977, 20, 1401.

[54] A. Ahrendts, Wärme-Stoffübertragung 1972, 5, 239.

[55] C. J. Hurst, D. R. Olson, J Heat Trans-T Asme 1973, 95, 12.

[56] F. M. White, *Fluid mechanics*, McGraw-Hill, New York 2008.

[57] C. Graham, P. Griffith, International Journal of Heat and Mass Transfer 1973, 16, 337.

[58] H. Tanaka, T. Tsuruta, International Journal of Heat and Mass Transfer 1984, 27, 327.

[59] D. Tam, V. von Arnim, G. H. McKinley, A. E. Hosoi, J Fluid Mech 2009, 624, 101.

[60] R. W. Schrage, Columbia University., New York, 1953, viii.

[61] N. Miljkovic, R. Enright, Y. Nam, K. Lopez, N. Dou, J. Sack, E. N. Wang, Nano Lett 2013, 13, 179.

[62] Y. Nam, Y. S. Ju, Journal of Adhesion Science and Technology 2013, 27, 2163.

[63] M.-K. Kim, H. Cha, P. Birbarah, S. Chavan, Zhong. C, Y. Xu, N. Miljkovic, Langmuir 2015, 31, 13452.

[64] K. Rykaczewski, J. H. J. Scott, A. G. Fedorov, Appl Phys Lett 2011, 98.

[65] Y. Zhou, W. Yi-Zhi, Y. Yi-Fan, G. Mao-Gang, X. Xiao-Liang, Chinese Physical Society 2012, 21.

[66] S. Necmi, J. W. Rose, International Journal of Heat and Mass Transfer 1977, 20, 877.

[67] J. W. Rose, International Journal of Heat and Mass Transfer 1969, 12, 233.

[68] W. J. Minkowycz, E. M. Sparrow, International Journal of Heat and Mass Transfer 1966, 9, 1125.

[69] D. Beysens, Atmospheric Research 1995, 39, 215.

[70] D. Beysens, C. M. Knobler, Phys Rev Lett 1986, 57, 5.

[71] D. Beysens, A. Steyer, P. Guenoun, D. Fritter, C. M. Knobler, Phase Transitions 1991, 31, 219.

[72] D. Kashchiev, *Nucleation - Basic Theory with Applications*, Butterworth-Heinemann, Great Britain 2000.

[73] J. P. Hirth, G. M. Pound, *Condensation and Evaporation - Nucleation and Growth Kinetics*, Pergamon Press, England 1963.

[74] R. Enright, N. Miljkovic, A. Al-Obeidi, C. V. Thompson, E. N. Wang, Langmuir 2012, 28, 14424.

[75] H. Mendoza, S. Beaini, V. P. Carey, J Heat Transf 2014, 136, 121501.

[76] L. Y. Barash, T. P. Bigioni, V. M. Vinokur, L. N. Shchur, Phys Rev E 2009, 79.

[77] S. S. Sadhal, M. S. Plesset, J Heat Trans-T Asme 1979, 101, 48.

[78] O. E. Ruiz, W. Z. Black, J Heat Trans-T Asme 2002, 124, 854.

[79] R. Enright, N. Miljkovic, A. Al-Obeidi, C. V. Thompson, E. N. Wang, Langmuir 2012, 40, 14424.